HUNIS: High-Performance Unsupervised Nuclei Instance Segmentation

Vasileios Magoulianitis
Electrical and Computer Engineering
University of Southern California
Los Angeles, CA, USA
magoulia@usc.edu

Yijing Yang
Electrical and Computer Engineering
University of Southern California
Los Angeles, CA, USA
yijingya@usc.edu

C.-C. Jay Kuo
Electrical and Computer Engineering
University of Southern California
Los Angeles, CA, USA
cckuo@sipi.usc.edu

ABSTRACT

A high-performance unsupervised nuclei instance segmentation (HUNIS) method is proposed in this work. HUNIS consists of two-stage block-wise operations. The first stage includes: 1) adaptive thresholding of pixel intensities, 2) incorporation of nuclei size/shape priors and 3) removal of false positive nuclei instances. Then, HUNIS conducts the second stage segmentation by receiving guidance from the first one. The second stage exploits the segmentation masks obtained in the first stage and leverages color and shape distributions for a more accurate segmentation. The main purpose of the two-stage design is to provide pixel-wise pseudo-labels from the first to the second stage. This self-supervision mechanism is novel and effective. Experimental results on the MoNuSeg dataset show that HUNIS outperforms all other unsupervised methods by a substantial margin. It also has a competitive standing among state-of-the-art supervised methods.

1 Introduction

Medical imaging is one of the fields that benefit a lot from the advancement of modern AI algorithms. They enable the computer aided diagnosis (CAD) tools to serve as physician's assistants. In particular, CAD in digital pathology becomes a fast growing area since it is conducive to cancer diagnosis and assessment. As part of this process, nuclei segmentation provides important visual cues, such as molecular morphological information [1] to expert pathologists.

Generally speaking, nuclei instance segmentation is an indispensable task in histology images reading for cancer assessment. Its automation is of high significance for pathologists' reading process. Hematoxylin and Eosin (H&E) staining has been used for years in histology to reveal the underlying nuclei structure. Variations along this process, especially for images coming from different laboratories that use different protocols and scanners, may affect nuclei color and texture. Manual segmentation of histology images carried out by expert pathologists is a labor-intensive and time-consuming task, also subject to high inter-observer variability [2]. Thus, a sufficiently large amount of annotated data is in paucity.

A high-performance unsupervised nuclei instance segmentation (HUNIS) method is proposed in this work. HUNIS consists of two-stage block-wise operations, where the first stage provides an initial segmentation result and yields pixel-wise pseudo-labels for the second stage. This self-supervision mechanism is novel and effective. It is shown by experimental results that HUNIS outperforms other unsupervised methods by a large margin. Besides, HUNIS is highly competitive with state-of-the-art supervised methods. The rest of the paper is organized as follows. Related work is reviewed in Sec. 2. HUNIS is presented in Sec. 3. Experimental results are shown in Sec. 4. Concluding remarks are given in Sec. 5.
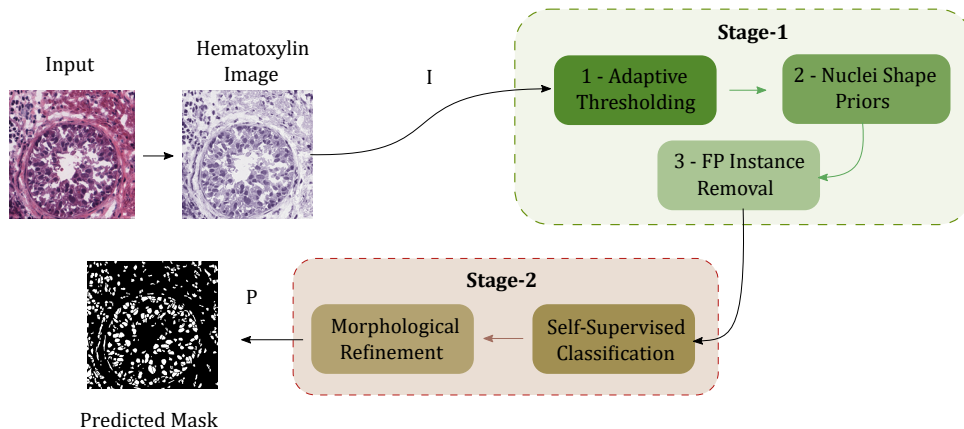
Figure 1: An overview of the proposed HUNIS method, where the first stage provides an initial nuclei segmentation result and yields pseudo-labels to guide the segmentation in the second stage.

2 Review of Related Work

Before the advent of the deep learning (DL) paradigm, earlier methods addressed this segmentation problem with no supervision. Examples include: Adaptive thresholding [3, 4, 5], clustering [6], active contours [7, 8], and graph cuts [9]. Another popular method is the watershed algorithm [10, 11], which is often used as a post-processing step, where research was mainly focused on finding proper markers to initialize the segmentation process.

In recent years, DL solutions are prevalent [12, 13, 14, 15, 16]. They attempt to handle multi-scale appearances of nuclei through separate branches of the networks and negative effects of hard samples through customized losses [17, 18, 14]. A self-supervised learning method was proposed by Sahasrabudhe *et al.* [19], that regularizes the encoder model implicitly with scale. Despite their effectiveness, it is challenging for DL models to generalize and transfer learned models from training to testing domains. Given the small-sized publicly available datasets and nuclei variations across different organs, DL solutions have their limitations.

Lately, unsupervised methods have shown promising performance on the nuclei instance segmentation task, e.g., [5, 20, 21, 22]. Among them, [20, 21, 22] are DL-based methods. [20] and [21] adopt domain adaptation and model regularization, while [22] uses generative adversarial networks (GANs) to synthesize histology images for the nuclei segmentation model. Yet, their performance is far inferior to that of supervised DL methods. On the other hand, the CBM method [5] is a non-DL solution, offering a transparent pipeline for addressing the problem and requiring no training data.

In this work, we devise a two-stage unsupervised processing pipeline, namely HUNIS. The first stage consists of a novel adaptive thresholding operation and a false positive (FP) nuclei removal module, to obtain an initial segmentation output. Then, the first stage's output is used to provide pixel-wise pseudo-label to guide the second stage processing for a more accurate segmentation. This self-supervision mechanism is novel and effective as demonstrated by experimental results in Sec. 4.

3 Proposed HUNIS Method

An overview of the proposed HUNIS method is shown in Fig. 1. It consists of a two-stage block-wise operations pipeline. The first stage includes: 1) adaptive thresholding of pixel intensity values, 2) incorporation of nuclei size/shape priors and 3) removal of false positive instances. The first stage provides an initial segmentation result and yields the pseudo-labels for self-supervising the second stage. The second stage exploits color and shape information under the self-supervised setting for a more accurate segmentation.

3.1 First-Stage Processing

3.1.1 Adaptive Thresholding

A histology image of size 1000×1000 is first decomposed into non-overlapping blocks of size 50×50 to ensure homogeneity at the local level. As a pre-processing step, we accentuate the foreground nuclei over background tissue,
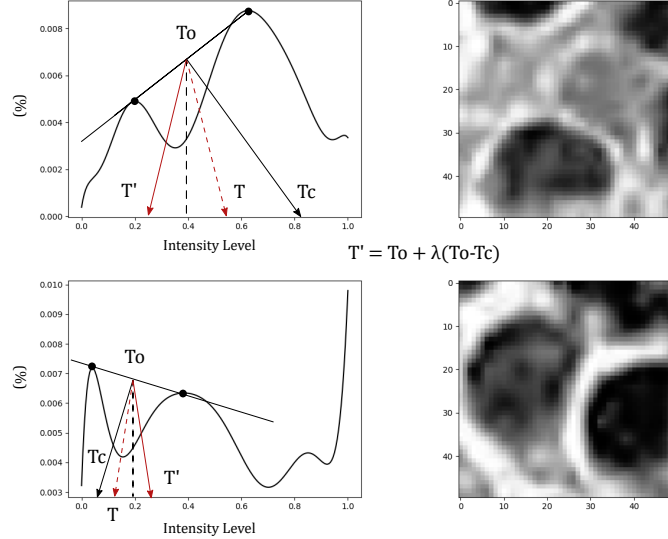
Figure 2: Two threshold adjustment scenarios: (top) a histogram of two imbalanced modalities and its corresponding block image and (bottom) a histogram of three modalities and its corresponding block image.

thus enhancing the subsequent adaptive thresholding operation. In general, the nuclei chromatic palette is mostly captured from Hematoxylin (H), in contrast with Eosin (E) that carries more information about the background. To this end, the original color image is projected on the H color basis using the approach described in [23]. A contrast enhancement is applied to the H-image to further highlight the nuclei. Next, color pixels are converted into monochrome ones within each block to facilitate the following thresholding operation. The color transformation can be achieved by applying principal component analysis (PCA) and retaining the first principal component, called the intensity value below. PCA removes the correlation among RGB channels and achieves high energy compaction. The L value in the LAB color space is used as reference to select the sign of the eigenvector at each block uniquely. The color-to-intensity transformation simplifies a color-based segmentation mechanism from 3D to 1D. While it works well for the majority of blocks, we consider color attributes in stage-2 to further increase the segmentation performance.

We conduct local thresholding on pixel intensities in each block adaptively based on a bi-modal assumption. That is, if the intensity histogram in a block has two main peaks, one corresponding to foreground and one to background, and the notch between the two peaks is low enough, one can choose the intermediate point between the two peaks point as a binarization threshold. There are however challenging cases where the bi-modal assumption is violated. Then, a mechanism is needed to adjust the threshold. Two such examples are shown in Fig. 2. They occur because of ambiguous instances with mid-level intensities (see the top case) or poor contrast between nuclei and background (see the bottom case).

The threshold is adjusted using the following algorithm. The peak points of the first and second modalities are shown by solid dots in the left two sub-figures of Fig. 2. The mid-point between the two is denoted by T_o. We draw a line that is perpendicular to the line segment formed by the two dots and passing through T_0. Its intercept, T_c, with the horizontal line of zero occurrence is used as a reference point for correcting the initial T_o. Then, we have

$$T' = T_o + \lambda(T_o - T_c), \quad 0 < \lambda < 1, \tag{1}$$

where T' is the adjusted threshold value and the second term on the left-hand-side is called a correction term. As shown in the top case of Fig. 2, if the second peak (i.e., background) is higher than the first one (i.e., nuclei), it is likely that the block has low contrast and ambiguous regions and it is desired to decrease T_o to reduce the false positive rate. On the other hand, as shown in the bottom case of Fig. 2, if the mid-peak is high but not higher than the first peak (i.e., nuclei), it is likely that the mid-modality region corresponds to nuclei boundaries (given the first peak being the nuclei) or due to its texture. Thus, we can increase T_o to segment nuclei more precisely.

The direction and magnitude of threshold adjustment is automatically determined from the slope of the line segment connecting the two dots. A positive slope would give an intercept, T_c, higher from T_o and the correction term in Eq. (1) is negative. Conversely, a negative slope would yield a positive correction. A weight, λ, is used to control the correction

amount, whose value is obtained empirically. Note that point T in Fig. 2 is the reflection of T' about the vertical line with intensity equal to T_o. It does not appear in Eq. (1) and it is drawn only for illustration purposes.

3.1.2 Incorporation of Size/Shape Priors

The output from the adaptive thresholding module is often noisy. Prior knowledge about nuclei size and shape can be incorporated to remove that noisy predictions at the instance level. To this end, we calculate the histogram of nuclei sizes in an image. Unusually small nuclei instances from unsupervised thresholding are perceived as noise and can be filtered out. Moreover, two or more close nuclei can end up being connected after segmentation because of unclear boundaries. Shape priors (e.g., nuclei shape convexity) can help split those falsely connected nuclei. Algorithmically, the convex hull algorithm can detect abnormally steep curves along nucleus boundary, indicating that the instance came after two or more bundled nuclei and so they can be split. Furthermore, hole filling is used to correct open areas in the interior of a nucleus and thus compensate for inner texture variations that challenge the thresholding operation.

3.1.3 Removal of False Positive Instances

Some false positive nuclei instances cannot be filtered out in the size/shape priors module. They usually come from darker background areas (resulting from defects in staining process) or small nuclei with ambiguous texture. We propose a simple and efficient way to reduce the false positive rate. In this module, we consider a larger local neighborhood, called a tile (say, of size 200×200) to include more detected instances for consideration. Each tile is processed independently. The idea is to compare instances that are more likely to be true positives with other ambiguous instances that could potentially be false positives. The size prior contributes here. Larger instances are less likely to be false positives while the chances for smaller instances to be falsely marked are higher. This is mainly due to the combined operation of adaptive threshoding and size/priors modules. Hence, we have a global nuclei size threshold to deduce what instances will be used as "ground truth" in a tile. To be more specific, we have two sets of instances: the reference instances set, R, and the query instances set, Q. All instances with sizes larger than a threshold are assigned to set R while the remaining ones to set Q. Each element in Q is compared against the mean ensemble of elements in R. If their similarity is poor, it is likely to be a FP instance and can be eliminated.

To evaluate the similarity and compare instances in R and Q, some attributes are extracted per instance. Since most instances from Q have lower contrast and poorer color saturation, we use HSV colorspace and the corresponding contrast value per instance as features to discern FP nuclei. For R class, we aggregate all instance features to yield one reference feature for comparison. That is, we extract the feature vector $\mathbf{x}_R$ by averaging their values of all instances in R via

$$\mathbf{x}_R = \frac{1}{|R|} \sum_{i \in R} \mathbf{x}_i, \tag{2}$$

where $\mathbf{x}_i$ is the feature vector of the i-th instance in R. Then, we compare the similarity of the same feature vector of a query sample against $\mathbf{x}_R$. The similarity metric is defined as:

$$S(\mathbf{x}_R, \mathbf{x}_j) = e^{-\gamma ||\mathbf{x}_j - \mathbf{x}_R||_2^2}, \quad \forall j \in Q, \tag{3}$$

where γ is a hyper-parameter. Clearly, $0 \leq S \leq 1$. The higher the S value, the higher the similarity. A query instance is removed, if its $S < T_S$, where T_S is another hyperparameter. The process of false-positive nuclei instance removal is illustrated in Fig. 3.

3.2 Second-Stage Processing

3.2.1 Self-Supervised Binary Classification for Uncertain Pixels

The nuclei color distribution in a tile is more stable than that in the entire image and gives richer information about nuclei appearance over background. As such, unlike stage-1 that carries out operations on monochrome patches, this module operates in tiles of 200×200 from the Hematoxylin image. We first train a classifier based on the pseudo-labels obtained from step-1 in a pixel-wise manner. Then, we conduct prediction for uncertain pixels, based on the classifier's confidence. Most of those pixels usually lie close to the nuclei boundaries. As long as the majority of pixel labels in a tile are correct, some of the noise in pseudo-labels can be removed and thus pixels are more likely to be assigned to their correct class. This implies that large and solid nuclei are more probable to stay intact, while some of the smaller instances or nuclei boundary areas can be corrected towards their correct class.

3.2.2 Shape Refinement

In this module, we perform a final round of nuclei shape refinement using the same priors and procedures as in its counterpart from Stage-1. Since pixel-wise classification is prone to false predictions to some extent, this module refines
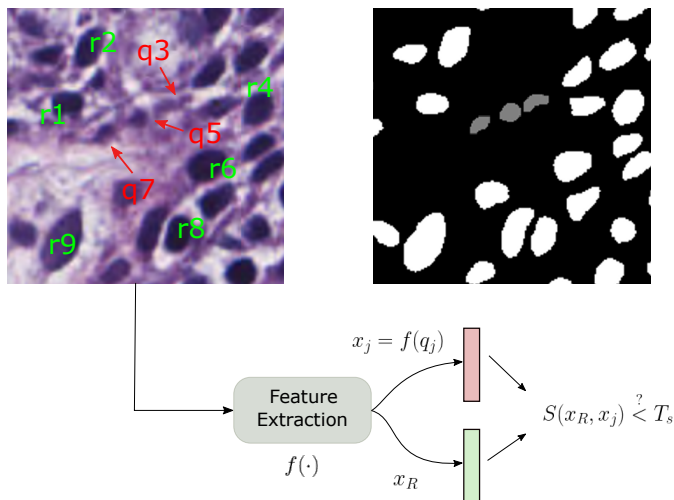
Figure 3: Illustration of the effect of the false positive removal module, where some small-sized instances (in red) are compared with larger instances (in green) that are more likely to be actual nuclei. The marked instances in grey (right sub-figure) have a similarity score below T_s and are eliminated.

the output so that it has a better segmented nuclei instance. This refinement is necessary since the shapes of some nuclei could be distorted after splitting or due to unclear boundaries. Thus, we preserve convexity using the convex hull algorithm for nuclei that have abnormally steep contours regions. Other morphological operations are also used to refine the nuclei shape.

4 Experimental Results

The proposed HUNIS method is evaluated on the 2018 MICCAI MoNuSeg dataset [12] to demonstrate its effectiveness. The dataset offers different testing protocols. For performance benchmarking, we follow the data splitting scheme as specified in [12]. That is, we report results on two MoNuSeg Challenge test datasets:

- 14 images from various organs whose histology images are available in the training dataset, here referred to as MoNuSeg Test-1.

- 6 histology images from three unseen organs (bladder, colon and stomach), referred to as MoNuSeg Test-2.

The parameters in Eqs. (1) and (3) are set to $\lambda = 0.3$ and $\gamma = 0.1$, respectively. The similarity threshold in Fig. 3 is set to $T_s = 0.6$. All other parameters are determined automatically from the data. For evaluation purposes, it is common among other works to use the Aggregated Jaccard Index (AJI) [12], rather than the F-1 score or the DICE coefficient. AJI is more suitable for instance-level segmentation tasks, since it takes both nuclei-level detection and pixel-level error performance into account.

The results for MoNuSeg Test-1 and Test-2 are shown in Tables 1 and 2, respectively. All benchmarking methods except CBM are DL-based. As shown in Table 1, one can see that HUNIS outperforms all DL unsupervised approaches by large margins in Test-1. It also outperforms CBM by 0.0245 in terms of the AJI score. Furthermore, HUNIS achieves a competitive standing among state-of-the-art supervised DL methods in Test-1. Its performance is close to that of the 2nd best in the table, namely, UNet-Atten. [16].

The domain adaptation task in Test-2 is quite challenging for supervised methods since they need to make a decision on data from unseen organ. As shown in Table 2, HUNIS outperforms all benchmarking unsupervised and supervised methods, including sophisticated DL models such as CIA-Net. Evidently, it is difficult for DL models to generalize well from training to testing when the amount of annotated data is scarce. In contrast, Test-1 and Test-2 make little difference for unsupervised methods. We see that HUNIS can achieve an even higher AJI score in Test-2 as compared with Test-1.

An ablation study that demonstrates the progressive improvement on segmentation results in various stages of HUNIS is given in Table 3. It shows the effectiveness of false positive instances removal module (Module 3 in Stage 1) and two modules in Stage 2. They contribute to significant AJI score improvement from the output of the previous stage.

Table 1: Quantitative results and performance comparison on Test-1 using AJI metric.

Method	AJI
Unsupervised	
DARCNN [21]	0.4461
Hou *et al.* [22]	0.4980
Self-Supervised [19]	0.5354
Liu *et al.* [20]	0.5610
CBM [5]	0.6142
HUNIS (ours)	**0.6387**
Supervised	
CNN3 [12]	0.5083
Hover-Net [14]	0.618
UNet-Atten. [16]	0.6498
NucleiSegNet [15]	**0.688**

Table 2: Quantitative results and performance comparison on Test-2 using the AJI metric.

Method	AJI
Unsupervised	
Cell Profiler [24]	0.0809
Fiji [25]	0.3030
CBM [5]	0.5808
HUNIS (ours)	**0.6548**
Supervised	
CNN3 [12]	0.4989
BES-Net [13]	0.5823
CIA-Net [17]	**0.6306**

It is worthwhile to stress that HUNIS does not carry any learnable parameters. In contrast, modern DL models typically contain millions of parameters. For example, the NucleiSegNet model and the UNet-Atten model take up 15.7M and 32M parameters, respectively. They need GPU to conduct the training and testing tasks. HUNIS can be implemented by software in mobile/edge devices. Furthermore, it is a fully unsupervised solution requiring no training data at all.

Table 3: Segmentation improvement over different stages of our pipeline in Test-2 set

Stages	Stage-1 (Modules 1&2)	Stage-1 (Modules 1&2&3)	Stages 1&2
AJI	0.6045	0.6377	0.6548

5 Conclusion and Future Work

An unsupervised nuclei instance segmentation method, namely HUNIS, was proposed in this work. It contains several novel ideas, such as an advanced adaptive thresholding scheme that can adjust the binarization threshold based on the local distribution automatically, an efficient false positive nuclei removal technique that can eliminate ambiguous instances, and a self-supervised learning mechanism that can finetune the segmentation results. Experimental results showed that HUNIS outperforms other unsupervised methods and maintains competitive performance against state-of-the-art supervised methods. It has no learnable parameters and it comes with very low computational complexity,

thus offering a green solution to the nuclei instance segmentation problem. It is interesting to extend the developed methodology to other relevant medical segmentation problems as well.

References

[1] Metin N Gurcan, Laura E Boucheron, Ali Can, Anant Madabhushi, Nasir M Rajpoot, and Bulent Yener. Histopathological image analysis: A review. *IEEE reviews in biomedical engineering*, 2:147–171, 2009.

[2] Juan C Caicedo, Allen Goodman, Kyle W Karhohs, Beth A Cimini, Jeanelle Ackerman, Marzieh Haghighi, CherKeng Heng, Tim Becker, Minh Doan, Claire McQuin, et al. Nucleus segmentation across imaging experiments: the 2018 data science bowl. *Nature methods*, 16(12):1247–1253, 2019.

[3] Jing-Hao Xue and D Michael Titterington. t-tests, f-tests and otsu's methods for image thresholding. *IEEE Transactions on Image Processing*, 20(8):2392–2396, 2011.

[4] Cheng Lu, Muhammad Mahmood, Naresh Jha, and Mrinal Mandal. A robust automatic nuclei segmentation technique for quantitative histopathological image analysis. *Analytical and Quantitative Cytology and Histology*, 34:296–308, 2012.

[5] Vasileios Magoulianitis, Peida Han, Yijing Yang, and C-C Jay Kuo. Unsupervised data-driven nuclei segmentation for histology images. *arXiv preprint arXiv:2110.07147*, 2021.

[6] Adel Hafiane, Filiz Bunyak, and Kannappan Palaniappan. Fuzzy clustering and active contours for histopathology image segmentation and nuclei detection. In *International Conference on Advanced Concepts for Intelligent Vision Systems*, pages 903–914. Springer, 2008.

[7] Khamael Al-Dulaimi, Inmaculada Tomeo-Reyes, Jasmine Banks, and Vinod Chandran. White blood cell nuclei segmentation using level set methods and geometric active contours. In *2016 International Conference on Digital Image Computing: Techniques and Applications (DICTA)*, pages 1–7. IEEE, 2016.

[8] Mohammed Ali Roula, Ahmed Bouridane, and Fatih Kurugollu. An evolutionary snake algorithm for the segmentation of nuclei in histopathological images. In *2004 International Conference on Image Processing, 2004. ICIP'04.*, volume 1, pages 127–130. IEEE, 2004.

[9] Hongming Xu, Lina Liu, Xiujuan Lei, Mrinal Mandal, and Cheng Lu. An unsupervised method for histological image segmentation based on tissue cluster level graph cut. *Computerized Medical Imaging and Graphics*, 93:101974, 2021.

[10] Pengfei Shen, Wenjian Qin, Jie Yang, Wanming Hu, Shifu Chen, Ling Li, TieXiang Wen, and Jia Gu. Segmenting multiple overlapping nuclei in h&e stained breast cancer histopathology images based on an improved watershed. In *2015 IET International Conference on Biomedical Image and Signal Processing (ICBISP 2015)*, pages 1–4. IET, 2015.

[11] Mitko Veta, A Huisman, Max A Viergever, Paul J van Diest, and Josien PW Pluim. Marker-controlled watershed segmentation of nuclei in h&e stained breast cancer biopsy images. In *2011 IEEE international symposium on biomedical imaging: from nano to macro*, pages 618–621. IEEE, 2011.

[12] Neeraj Kumar, Ruchika Verma, Sanuj Sharma, Surabhi Bhargava, Abhishek Vahadane, and Amit Sethi. A dataset and a technique for generalized nuclear segmentation for computational pathology. *IEEE transactions on medical imaging*, 36(7):1550–1560, 2017.

[13] Hirohisa Oda, Holger R Roth, Kosuke Chiba, Jure Sokolić, Takayuki Kitasaka, Masahiro Oda, Akinari Hinoki, Hiroo Uchida, Julia A Schnabel, and Kensaku Mori. Besnet: boundary-enhanced segmentation of cells in histopathological images. In *International Conference on Medical Image Computing and Computer-Assisted Intervention*, pages 228–236. Springer, 2018.

[14] Simon Graham, Quoc Dang Vu, Shan E Ahmed Raza, Ayesha Azam, Yee Wah Tsang, Jin Tae Kwak, and Nasir Rajpoot. Hover-net: Simultaneous segmentation and classification of nuclei in multi-tissue histology images. *Medical Image Analysis*, 58:101563, 2019.

[15] Shyam Lal, Devikalyan Das, Kumar Alabhya, Anirudh Kanfade, Aman Kumar, and Jyoti Kini. Nucleisegnet: robust deep learning architecture for the nuclei segmentation of liver cancer histopathology images. *Computers in Biology and Medicine*, 128:104075, 2021.

[16] Jo Schlemper, Ozan Oktay, Michiel Schaap, Mattias Heinrich, Bernhard Kainz, Ben Glocker, and Daniel Rueckert. Attention gated networks: Learning to leverage salient regions in medical images. *Medical image analysis*, 53:197–207, 2019.

[17] Yanning Zhou, Omer Fahri Onder, Qi Dou, Efstratios Tsougenis, Hao Chen, and Pheng-Ann Heng. Cia-net: Robust nuclei instance segmentation with contour-aware information aggregation. In *International Conference on Information Processing in Medical Imaging*, pages 682–693. Springer, 2019.

[18] Xinpeng Xie, Jiawei Chen, Yuexiang Li, Linlin Shen, Kai Ma, and Yefeng Zheng. Instance-aware self-supervised learning for nuclei segmentation. In *International Conference on Medical Image Computing and Computer-Assisted Intervention*, pages 341–350. Springer, 2020.

[19] Mihir Sahasrabudhe, Stergios Christodoulidis, Roberto Salgado, Stefan Michiels, Sherene Loi, Fabrice André, Nikos Paragios, and Maria Vakalopoulou. Self-supervised nuclei segmentation in histopathological images using attention. In *International Conference on Medical Image Computing and Computer-Assisted Intervention*, pages 393–402. Springer, 2020.

[20] Dongnan Liu, Donghao Zhang, Yang Song, Fan Zhang, Lauren O'Donnell, Heng Huang, Mei Chen, and Weidong Cai. Unsupervised instance segmentation in microscopy images via panoptic domain adaptation and task re-weighting. In *Proceedings of the IEEE/CVF conference on computer vision and pattern recognition*, pages 4243–4252, 2020.

[21] Joy Hsu, Wah Chiu, and Serena Yeung. Darcnn: Domain adaptive region-based convolutional neural network for unsupervised instance segmentation in biomedical images. In *Proceedings of the IEEE/CVF Conference on Computer Vision and Pattern Recognition*, pages 1003–1012, 2021.

[22] Le Hou, Ayush Agarwal, Dimitris Samaras, Tahsin M Kurc, Rajarsi R Gupta, and Joel H Saltz. Robust histopathology image analysis: To label or to synthesize? In *Proceedings of the IEEE/CVF Conference on Computer Vision and Pattern Recognition*, pages 8533–8542, 2019.

[23] Paula Andrea Dorado, Raul Celis, and Eduardo Romero. Color separation of h&e stained samples by linearly projecting the rgb representation onto a custom discriminant surface. In *12th International Symposium on Medical Information Processing and Analysis*, volume 10160, page 101600P. International Society for Optics and Photonics, 2017.

[24] Anne E Carpenter, Thouis R Jones, Michael R Lamprecht, Colin Clarke, In Han Kang, Ola Friman, David A Guertin, Joo Han Chang, Robert A Lindquist, Jason Moffat, et al. Cellprofiler: image analysis software for identifying and quantifying cell phenotypes. *Genome biology*, 7(10):1–11, 2006.

[25] Johannes Schindelin, Ignacio Arganda-Carreras, Erwin Frise, Verena Kaynig, Mark Longair, Tobias Pietzsch, Stephan Preibisch, Curtis Rueden, Stephan Saalfeld, Benjamin Schmid, et al. Fiji: an open-source platform for biological-image analysis. *Nature methods*, 9(7):676–682, 2012.